Computational Biomechanics of the Distal Tibia from High-Resolution MR and Micro-CT Images

Chamith S. Rajapakse[1], **Jeremy F. Magland**[1], **Michael J. Wald**[1], **X. Sherry Liu**[2], **X. Henry Zhang**[2], **X. Edward Guo**[2], and **Felix W. Wehrli**[1]

Chamith S. Rajapakse: chamith@mail.med.upenn.edu; Jeremy F. Magland: jeremy.magland@gmail.com; Michael J. Wald: waldm@seas.upenn.edu; X. Sherry Liu: xl2014@columbia.edu; X. Henry Zhang: xz2107@columbia.edu; X. Edward Guo: ed.guo@columbia.edu; Felix W. Wehrli: wehrli@mail.med.upenn.edu

[1]Laboratory for Structural NMR Imaging, Department of Radiology, University of Pennsylvania, Philadelphia, Pennsylvania, USA

[2]Bone Bioengineering Laboratory, Department of Biomedical Engineering, Columbia University, New York, New York, USA

Abstract

The mechanical properties of bone estimated by micro-finite element (µFE) analysis on the basis of *in-vivo* micro-MR images (µMRI) of the distal extremities provide a new tool for direct assessment of the mechanical consequences of intervention. However, the accuracy of the method has not previously been investigated. Here, we compared µFE-derived mechanical parameters obtained from µMR images at 160 µm isotropic voxel size now achievable *in vivo* with those derived from 25 µm isotropic (reference) µCT images of thirty cadaveric tibiae from fifteen donors (4 females, 11 males, 55–84 yrs.). Elastic and shear moduli estimated from $(5 \text{ mm})^3$ sub-volumes of trabecular bone (TB) derived from µMR images were significantly correlated with those derived from volume-matched reference µCT images ($R^2 = 0.60$–0.67). Axial stiffness of whole-bone sections (including both cortical and trabecular compartments) derived from µMR-based models were highly correlated ($R^2 = 0.85$) with those from high-resolution reference images. Further, µFE models generated from µCT images after downsampling to lower resolutions relevant to *in-vivo* µMRI (100–160 µm), showed mechanical parameters to be strongly correlated ($R^2 > 0.93$) with those derived at reference resolution (25 µm). Incorporation of grayscale image information into the µMR-based µFE model yielded slopes closer to unity than binarized models (1.07 ± 0.15 vs. 0.71 ± 0.11) when correlated with reference sub-regional elastic and shear moduli. The work suggests that elastic properties of distal tibia can be reliably estimated by µFE analysis from µMR images obtainable at *in-vivo* resolution.

Keywords

Micro-MRI; Bone Biomechanics; Trabecular Bone; Cortical Bone; Finite-Element Analysis; Bone Stiffness

Corresponding Author: Chamith S. Rajapakse, Ph.D., Department of Radiology, University of Pennsylvania, 1 Founders, 3400 Spruce Street, Philadelphia, PA 19104, U.S.A., chamith@mail.med.upenn.edu, Phone : 215-349-8519, Fax : 215-662-7263.

Introduction

The success of osteoporosis management strategies hinges on both the predictability of bone's fracture risk and detectability of treatment efficacy. Currently, such assessments are based on bone-mineral density (BMD), typically quantified with dual-energy X-ray absorptiometry (DXA), at the spine or proximal femur. However, BMD measurements often fail to predict fractures[1,2] and a significant number of people classified as osteoporotic (BMD T-score <-2.5)[3] do not actually sustain fractures.[4] Furthermore, short-term BMD tests are not very useful in tracking treatment efficacy, because of the inability of BMD to detect structural changes that do not significantly alter overall bone mass.

The less-than-satisfactory performance of DXA-based BMD measurements in predicting fracture susceptibility and monitoring response to treatment have spurred the search for other markers of bone quality. Micro-magnetic resonance imaging (µMRI) and high-resolution peripheral quantitative computed tomography (HR-pQCT) are two emerging technologies with potential for assessment of bone quality. Both modalities are able to produce *in-vivo* images adequate to at least partially resolve trabecular bone (TB) micro-structure at the distal extremities (radius,[5,6] tibia,[5,6] and calcaneus [7,8]). Images produced by these two modalities have also been shown to be suitable for the generation of micro-finite element (µFE) models that allow estimation of mechanical properties of bone such as stiffness and failure strength.[9,10] Furthermore, the ability of µFE modeling to track short-term changes in mechanical properties in response to treatment has also been demonstrated, even in the absence of any detectable changes in either BMD or bone-volume fraction (BV/TV).[11,12]

The validity of mechanical parameters estimated on the basis of high-resolution image-derived µFE analysis has been well established in comparison to actual mechanical testing of TB specimens.[13,14] Furthermore, high-resolution (~10 µm) micro-computed tomography (µCT) has been widely considered as the gold standard for generating µFE models of TB due to its ability to faithfully resolve the micro-structure.[15] On the other hand, the resolutions achievable by *in-vivo* bone imaging modalities are considerably lower due to limitations imposed by signal-to-noise ratio (SNR) in µMRI and radiation dose in HR-pQCT. Typical *in-vivo* voxel sizes are on the order of $(80 \mu m)^3$ and $(160 \mu m)^3$ for HR-pQCT and µMRI, respectively. However, the actual resolutions of the two *in-vivo* modalities have been argued to be comparable on the basis of point-spread function characteristics.[10] While the implications of limited resolution (and SNR) on mechanical parameters derived from µMRI-based µFE analysis have been demonstrated,[10] the accuracy of such estimates has not previously been investigated on the basis of isotropic µMR images (160 µm) acquired using pulse-sequence parameters (TE/TR, scan time, etc.) now possible for *in-vivo* imaging of the extremities.[16]

Even though the feasibility of analyzing µFE models generated from high-resolution images of whole cross-sections has been demonstrated using highly parallel supercomputer systems, [17] the computational and memory demands imposed by µFE solvers have limited the analysis, thus far, on typical desktop computer systems, to TB sub-regions on the order of 1 cm^3.[10,12] Furthermore, the practicality of quantifying the relative contributions of cortical bone (CB) and TB compartments to overall bone stiffness at the distal extremities using µMRI-based µFE has not previously been addressed.

The main goal of the present work is to demonstrate the feasibility and practicality of µMR-based µFE estimates of bone mechanical competence at resolutions achievable *in vivo*. Towards this objective, we have conceived and implemented a µFE-analysis framework that can take grayscale images as input and generate mechanical parameters –stiffness, elastic

moduli, and shear moduli-- of bone in the distal extremities. The accuracy of the µMR-derived mechanical parameters was established by comparison with those derived from high-resolution µCT images of cadaveric distal tibia specimens serving as a reference. Lastly, to support the notion that TB and CB compartments act synergistically to confer strength, we estimated bone stiffness with and without the cortex.

Materials and Methods

Image Acquisition

Thirty human distal tibia specimens of 25 mm length in axial direction, encompassing the distal metaphysis, were obtained from cadavers of fifteen donors (four females and eleven males; 55–85 years). Micro-CT images from the center 10 mm region were subsequently obtained (µCT 80, Scanco Medical, Switzerland) at 25 µm isotropic voxel size with marrow *in situ* (Figure 1). Subsequently, bone marrow was removed using a water jet and the specimens were immersed in 10% aqueous formalin doped with 1 mM Gd-DTPA to shorten the longitudinal relaxation time (T_1) to ~300 ms commensurate with fatty marrow (*ex-vivo* specimen imaging demands removal of marrow since air inclusions cause magnetic susceptibility and signal drop-out artifacts).[18] The specimens were then centrifuged at 2000 rpm for 5 minutes to remove remaining air trapped in the inter-trabecular spaces. Finally, 3D µMR images from the center 20 mm region in axial direction of the specimens were acquired (imaging time ~40 min) on a clinical 1.5 Tesla scanner (MAGNETOM Sonata, Siemens Medical Solutions, Germany) with a custom-built receive-only phased-array radiofrequency surface coil at 160µm isotropic voxel size using a variant of the 3D FLASE (fast large angle spin echo pulse) sequence.[19]

Image Processing

Figure 1 schematically describes the preprocessing steps needed to extract common 3D volumes from µMR and µCT (reference) images for validation purposes. Bone regions of high-resolution µCT images were first segmented by setting a threshold at the midpoint between the peaks of bone and marrow in the voxel intensity histogram. For µMR images, the signal variations across the volume produced by inhomogeneous sensitivity of the receive coil were first corrected using a local thresholding algorithm.[20] Subsequently, µMR images were co-registered to µCT images using a rigid-body registration algorithm by maximizing the cross correlation between images.[21] Finally, common 5 mm × 5 mm × 5 mm subvolumes were extracted from the center of the TB region for analysis.

Micro-Finite-Element Modeling of TB Sub-Regions

The macroscopic mechanical properties (of the selected region), were computed by µFE analysis using custom-designed software.[22,23] The µFE model largely follows that proposed by van Rietbergen et al.[24] for µCT-based analysis and was extended to allow for input of grayscale µMR and µCT images. The grayscale pixel values of the selected image volume were linearly scaled to cover the range from 0 to 100 with pure 'marrow' and pure bone having minimum and maximum values, respectively. We refer to the resulting 3D array as the bone-volume-fraction (BVF) map with entries representing the percentage of the voxel occupied by bone. Each voxel in the BVF map was directly converted to a hexahedral (brick) finite element with dimensions corresponding to image voxel size. The bone tissue material properties were chosen as isotropic and linearly elastic with each element's Young's modulus (YM) set to be linearly proportional to the BVF value (BVF-scaled) such that YM = (15 GPa) × (BVF) while the Poisson's ratio was kept constant at 0.3 for all elements. Each finite-element vertex (node) was assumed to have three degrees of freedom corresponding to displacements along x, y, and z axes in the image coordinate. Hence, the number of free variables in the model is $3(N_1 + 1)(N_2 + 1)(N_3 + 1)$, where $N_1 = N_2 = N_3 =$

63 (array size) for the 1 cm^3 sub-volume. The nodes surrounded by 8 elements with zero BVF values were excluded from the model. An empirically found partial threshold was applied by setting elements with BVF<20% to zero in order to remove the contributions from image noise.

Simulated Compression and Shear Testing of Cubic Sub-Volumes

To estimate the mechanical properties from the generated µFE model, the macroscopic relationship between stress and strain had to be determined. The macroscopic elastic and shear moduli were calculated by simulating compression and shear testing on the µFE model by imposing different boundary conditions on the eight surfaces of the modeled bone region. The elastic moduli (E_{11}, E_{22}, and E_{33}) along each of the three principal axes of the image coordinate system (x, y, and z) were found by performing three 'compressive' tests along each of the axes. The value of E_{11}, for example, was obtained by simulating a small displacement (compressive strain ~1%) along the × direction to all nodes on one of the boundary surfaces perpendicular to the x axis (x=0) in such a manner that the nodes on the opposite surface (x=N_1) are restrained along the x direction while lateral displacements remain unrestrained. Such a boundary condition yields $3(N_1 - 1)(N_2 + 1)(N_3 + 1) + 2(N_2 + 1)(N_3 + 1)$ free variables corresponding to the displacements of unrestrained nodes and displacements along y and z directions for the restrained nodes. The unknown displacements at each node can then be found by minimizing the total strain energy of the system. Subsequently, the resulting stress along the x direction was calculated by summing the x components for the reaction force on the x=0 surface and dividing by the surface area. Finally, E_{11} was estimated as the ratio of calculated stress to the applied strain. Analogously, E_{22} and E_{33} were also obtained. Using a similar approach, shear moduli (G_{23}, G_{31}, and G_{12}) of the modeled region were estimated by simulating shear displacements applied to nodes on opposite surfaces along anti-parallel directions.

Evaluation of the Effect of Resolution

To evaluate the dependence of mechanical properties on image resolution, µFE simulations were performed on the basis of segmented µCT images, serving as an approximation to the ground truth. High-resolution µCT images (25-µm isotropic voxel size) were first binarized at the midpoint between the peaks of bone and marrow intensities of the histogram and subsequently resampled to 100, 120, 140, and 160 µm isotropic voxel sizes while retaining the grayscale information resulting from partial-volume mixing. Subsequently, BVF maps were generated for each of the datasets and common (5 mm)^3 cubic TB regions were subjected to µFE analysis by directly converting each voxel into a finite element as described above. Mechanical parameters resulting from 25 µm images were taken as the ground truth. FE computations were carried out on a laboratory computer system (dual quad core Xeon 3.16 GHz CPUs equipped with 28 GB of RAM). Further, to evaluate whether 25-µm µCT images can sufficiently resolve the trabeculae, intensity histograms were examined for bimodality (minimal partial-volume mixing). In addition, trabecular thickness (Tb.Th) was computed within the same sub-volumes used for µFE analysis as input. Tb.Th was computed with a 3D fuzzy distance transform technique previously shown to provide accurate results even in the presence of significant partial volume effects.[25]

Evaluating the Effect of Retaining Grayscale Information

To evaluate the importance of retaining grayscale image information once the voxel size approaches Tb.Th, µFE analysis was performed on the basis of both BVF-scaled and binarized µMR images. First, BVF maps (with each voxel being assigned a value ranging from 0–100) of 5 mm × 5 mm × 5 mm TB sub-volumes were binarized by using an empirically determined constant threshold. Next, two sets of computations were performed

as detailed above by taking µFE models generated from BVF-scaled and binarized images as input resulting in elastic and shear moduli.

Estimation of Whole-Bone Sectional Axial Stiffness

The µFE technique described above, which so far has been limited to a small sub-region of TB, was extended to estimate the stiffness of the entire cross-section of the distal tibia in the infero-superior (principal loading) direction. First, µFE models were generated, as detailed above, for common whole-bone sections selected from 160-µm µMR and reference µCT (25-µm) images. Simulated compression was applied along the principal loading direction (i.e. the bone's longitudinal axis) by applying a constant displacement (~1% strain) to all FE nodes in the proximal face of the finite element mesh while keeping those in the distal face constrained. The µFE system was solved as described above yielding a 3D strain map for the whole-bone section. Finally, the µMR-based axial stiffness obtained as the ratio of the applied strain on the proximal face to the resulting stress was compared to those derived from reference µCT images.

Estimation of Cortical and Trabecular Bone Stiffness

The synergy between CB and TB in providing the overall structural competence can be understood by analyzing the axial whole-bone-sectional axial stiffness of the two compartments both individually and together. First, the CB and TB compartments of the µMR-based BVF maps (generated as described above) were first segmented by delineating the periosteal and endosteal boundaries by an operator-guided region selection program developed in the authors' laboratory.[23] The segmentation resulted in three datasets for each specimen corresponding to CB, TB, and combined regions. Eight-millimeter sections along bone's principal loading direction were then extracted for µFE analysis. Finally, axial stiffness of each compartment along the principal loading direction was computed as detailed above.

Statistical Analysis

After testing for normality using Chi-square test, all correlations of mechanical and structural parameters were evaluated by least-squares regression in terms of the Pearson correlation coefficient using JMP Discovery Software (Version 7.02, SAS Institute, Inc.).

Results

Registration of µMR and µCT Images

The 3D rigid-body registration between µMR (160 µm) and µCT (25 µm) images produced closely matched ROIs. As visually evident from Figure 2, the BVF maps derived from registered µMR images bear close similarity with those obtained by µCT in both CB and TB regions.

Sub-Regional Elastic and Shear Moduli

Figure 3 displays elastic and shear moduli of cubic sub-volumes of TB computed from µMR images at voxel sizes achievable *in vivo* (160 µm isotropic), showing these to be significantly correlated (R^2 0.60–0.67) with those derived from volume-matched µCT (25 µm isotropic) images. The models generated from µCT and µMR images averaged 0.74±0.37 million and 2900±2000 finite elements, respectively. The convergence time for µCT and µMR-based models were 100±31 minutes and 6.0±0.30 seconds, respectively.

Effect of Resolution on μFE-Derived Mechanical Parameters

As can be seen from Table 1 and Figure 4, increased voxel size (100–160 μm) causes deviations of mechanical parameters compared to those obtained using reference μCT images at 25 μm. However, the deviations from ground truth values are highly predictable ($R^2>0.93$) for all six mechanical parameters even at the largest simulated voxel size (160 μm isotropic), which equals the voxel size now achievable by *in-vivo* μMRI.[26] Furthermore, the deviations are less for the elastic modulus along the longitudinal loading (E_{33}) than for transverse directions (E_{22} and E_{33}). Finally, we note that Tb.Th computed on the basis of highest resolution μCT images shows the image voxel size (25 μm) to be considerably below the trabecular bone thickness (40–105 μm), thereby justifying the use of these images and the derived mechanical parameters as representative of ground truth. The structural properties (BV/TV and Tb.Th) of the TB sub-regions used for the FE computation are listed in Table 2.

Effect of Retaining Grayscale Information

The sub-regional elastic and shear moduli derived from μMR images at 160 μm using BVF-scaled and binary models showed significant correlations with those obtained from high-resolution μCT images at 25 μm (R^2 0.60–0.67 and 0.50–0.68, respectively). However, the BVF-scaled models yielded slopes closer to unity (1.07±0.15 vs. 0.71±0.11 for those derived from the binary models), suggesting that the incorporation of grayscale image information into the μFE model increases the accuracy of derived mechanical parameters at resolutions typical of *in-vivo* μMRI.

Whole-Bone Sectional Axial Stiffness

Figure 5 displays the axial stiffness of whole-bone sections computed from μMR images at voxel sizes achievable *in vivo* (160 μm isotropic), showing high correlation with those derived from volume-matched μCT (25 μm isotropic) images ($R^2 = 0.85$). The μCT and μMR based intact (composite) models averaged 8.7±2.7 million and 39,000±12,000 finite elements, respectively. The convergence time for μCT and μMR-based models were 8.9±2.6 hours and 86±53 seconds, respectively.

Cortical and Trabecular Bone Stiffness

Based on the μMR images of the thirty tibia specimens, the mean stiffness of the CB was larger than that of the TB compartments (389±157 kN versus 310±178 kN). Mean stiffness of the isolated CB and TB compartments was 43±15% and 32±12%, respectively, of the values predicted for the intact model (927±397 kN). Whole-bone sectional stiffness of the intact bone comprising both compartments was 25±6% greater than the sum of stiffness values of the individual compartments (Figure 6a). Interestingly, the additional gain in stiffness of intact bone was highly correlated with the stiffness of the TB compartment ($R^2 = 0.50$, *p* = 0.0001) but there was no correlation with the stiffness of the cortical shell. Furthermore, when joined, stiffness correlated more strongly with TB than CB compartment (R^2 0.67 versus 0.38) as illustrated in Figure 6b.

Discussion

We investigated the accuracy of mechanical parameters obtained from BVF-scaled μMRI-based μFE analysis of bone at resolutions achievable *in vivo* by comparison to those derived from high-resolution reference μCT images of human distal tibia specimens. Additionally, the predictability of whole-bone sectional axial stiffness from individual contributions representing CB and TB compartments as well as the effect of resolution and grayscale information on parameters computed at typical *in vivo* resolutions were studied.

In vivo µMR images of bone are characterized by considerably lower resolution and SNR than those obtainable by high-resolution µCT of cadavers due to practical limitations in scan time. Nevertheless, within the range of SNR levels achievable *in vivo*, the derived mechanical parameters have previously been shown to be remarkably immune to noise.[21] In this work, we investigated the effect of limited resolution on µFE parameters derived from µMR images acquired with pulse-sequence parameters and at voxel volumes that have recently been shown to be feasible with *in vivo* bone micro-imaging[19] and compared the data with those obtained from reference µCT images. Elastic and shear moduli of TB estimated from the µMR images were significantly correlated (R^2 0.60 – 0.67) with those derived from µCT images (Figure 3), thus suggesting the feasibility of *in-vivo* assessment of mechanical properties of bone. We note that the R^2 values were somewhat lower for inter-modality correlations based on actual images compared to those derived from simulated images at 160 µm, possibly due to relatively small volume of trabecular bone (5 mm)^3 analyzed and as a result of errors in selecting identical TB sub-regions from the dual-modality images. Additionally, interpolation of µMR images (160 µm) for the purpose of 3D registration may also have contributed to reduced strength of the inter-modality correlations. Overall, however, simulations show that increased voxel size causes systematic overestimation of mechanical parameters compared to the reference values (Figure 4), resulting from artificial connections being introduced into the TB network once voxel dimensions approach and exceed those of trabecular thickness and spacing. Nevertheless, the correlation between mechanical parameters derived on the basis of simulated low-resolution images remains strong ($R^2 > 0.93$) compared to the reference high-resolution (25 µm) values even at the voxel sizes (160 µm) achievable by *in-vivo* µMRI. The data therefore suggest that the relative mechanical competence of bone in patients[12] can reliably be evaluated over a large range of bone-volume fraction and structural characteristics. Finally, we note that the degree of parameter overestimation at lower resolutions has a directional dependence, being least for the major loading direction. This observation can be explained by E_{33} being largely determined by the trabeculae oriented along the principal loading direction of the distal tibia, thus, within limits, lowering resolution along this direction, will not substantially affect recovery of these trabeculae.

The work also highlights the potential benefits of using grayscale information rather than generating the µMR-based µFE models from binarized images as segmentation of images acquired in the limited spatial resolution regime of *in-vivo* imaging always entails significant errors. All 3D reconstructions of µMR images of bone contain a range of grayscale values resulting from partial volume effects. We incorporated the grayscale information into the µFE models by linearly scaling the tissue moduli assigned to each finite element by the voxel BVF. Most notably, the BVF-scaled µFE models yielded elastic moduli much closer to the reference values than those obtained by setting a threshold in the images. Homminga et al. previously demonstrated the importance of using grayscale image information for generating µFE models of TB at different voxel sizes using µCT images,[27] showing that grayscale µFE models produce mechanical parameters superior to those derived from binary images, especially when the voxel dimensions are on the order of trabecular thickness. MacNeil et al. used attenuation values extracted from HR-pQCT images of cadaver forearms to scale local tissue modulus when generating µFE models of bone, showing a slight improvement in the accuracy of estimated stiffness and strength values.[28] Our data show that the incorporation of grayscale information of µMR images of bone into µFE models can also improve the accuracy of the estimated mechanical parameters at resolutions achievable *in vivo*.

Even though most osteoporotic fractures occur at skeletal locations rich in TB the overall strength of bone depends on the integrity of both cortex and TB. Here, we showed the feasibility of estimating whole-bone-sectional axial stiffness of the distal tibia via µMRI-

based μFE analysis in reasonable computation times on a laboratory computer system. Even though the cortex is known to contribute 45–75% of the bone strength,[29] the ability to quantify the relative contributions of the two compartments from μMR-based μFE analysis of extremities has not previously been investigated. After segmentation of the cortical shell from TB and quantification of the stiffness of individual compartments, we found overall axial stiffness to exceed the sum of stiffness values of the individual compartments by 25±6%, emphasizing the synergistic role of CB and TB in load bearing. The data also showed that the *interaction stiffness* (additional stiffness resulting from the interaction between the two compartments) increases with the elevated stiffness in the TB compartment ($R^2 = 0.50$, r<0.0001). On the other hand, the CB stiffness was not correlated to the interaction stiffness. This observation can be understood by analyzing the way TB is connected to the cortex at the endosteal boundary. While greater trabecular number and thickness enhance the stiffness of the TB compartment, one could argue that such a trend would be paralleled by a greater number of (stronger) connections to the endosteal cortical wall, and thus result in increased interaction stiffness relative to TB of lower trabecular number and thickness. The main contributor to the CB stiffness, on the other hand, is the thickness of the cortical shell, which has no direct influence on the number of connections to the TB compartment; therefore variations in CB stiffness not necessarily contribute to the variations in interaction stiffness.

Imaging capabilities are now available to obtain highly resolved isotropic μMR images of entire cross-section of distal extremities [16] which make the *in-vivo* assessment of individual compartmental stiffness and interaction stiffness feasible via μFE analysis. Trabeculae that connect to the endosteal cortical wall play an important role in re-routing load from cortex to trabecular bone compartment and vise versa, especially when the temporal changes in the two compartments are disproportionate. One such example is rapid cortical thinning prevalent in subjects with chronic kidney disease.[30] Therefore, the ability to measure strength of the interaction between the trabecular and cortical bone compartment (as indicated by interaction stiffness) *in vivo* could provide additional information about possible reduction in overall fracture risk of bone.

The estimation of the cross-sectional area of CB in the distal tibia (required for the computation of the macroscopic compressive modulus) is challenging, especially when the cortex is very thin -- on the order of voxel size. Therefore, stiffness (instead of modulus) was used as the primary mechanical parameter for the comparison of whole-bone sectional mechanical properties of the thirty tibia specimens.

Osteoporosis treatments – alendronate, parathyroid hormone, etc. -- are known to affect the CB and TB compartments differently.[31] Recently, Keaveny et al. showed that the femoral strength improvement following treatment, quantified using QCT-based FE analysis, is dominated by changes in the TB rather than the CB compartment.[32] Our data suggest that μMRI-based μFE analysis may be useful for noninvasive quantification of axial stiffness of the CB and TB compartments at extremities, thereby providing insight into the poorly understood relative biomechanical significance of the two compartments.

Some limitations of the study are noted. Currently, *in-vivo* μMRI (as well as HR-pQCT) is able of producing images with sufficiently resolved micro-structure of TB only at peripheral anatomic sites. Therefore, the validation study was performed on the basis of specimens extracted from distal tibia, which is a load-bearing surrogate site with a highly anisotropic trabecular network not dissimilar to vertebral bone. Even though the usefulness of nonlinear-μFE analysis in predicting bone strength has been demonstrated,[33] we confined our work to the linear-elastic regime due to current computational limitations on desktop computer systems. Furthermore, μFE analysis of trabecular bone and whole cross-section was limited

to relatively small sub-regions in order to keep scan time tolerable *in vivo* and also to allow the computations to be performed on a high-end desktop computer system. Nevertheless, a previous translational patient study with a similar scan protocol (albeit with highly anisotropic voxels) has shown µMRI-based µFE analysis to detect alterations in mechanical properties in response to treatment from a comparably sized sub-region.[12] Even though the tibia specimens included more male than female donors, we note that both BV/TV and elastic moduli covered a wide range of bone quality expected in healthy and osteoporotic men and women. BV/TV ranged from 1% – 18% and elastic modulus varied by more than two orders of magnitude (13 MPa – 1500 MPa).

A fundamental difference in the nature of µMR compared to µCT images has to be emphasized. Because the signal producing entity is bone marrow, µMR images do not provide bone-mineral density values. Therefore, currently, variations in tissue mineralization cannot be taken into account when generating the µFE model. Nevertheless, recent advances in ultrashort echo-time radial MR imaging have shown potential for quantifying bone mineral and matrix properties *in situ*.[34,35]

Finally, E_{11}, E_{22}, E_{33}, G_{23}, G_{31}, and G_{12} represent the elastic and shear moduli of TB sub-regions relative to the image coordinate axes (rather than along the axes with best orthotropic symmetry[24]). However, because the z-axis of the image coordinate system was aligned to a high degree with the infero-superior direction (which coincides with the direction of principal trabecular orientation in the distal metaphysis) during imaging the estimated mechanical parameters should not deviate significantly from those computed relative to orthotropic axes.[10,12] Lastly, the focus of this study was to evaluate intermodality agreement of mechanical parameters; therefore, as long as the images are cross-registered, the comparison is valid.

In summary, the present work indicates the feasibility of estimating mechanical properties of distal tibia on the basis of µMR images obtained at *in-vivo* resolution in good agreement with results from µFE modeling at much higher resolution. Application of the method for assessing the structural implications of drug intervention in patients undergoing high-resolution MRI in conjunction with computational biomechanics has recently been demonstrated in the authors' laboratory.[36] Lastly, the key question to be addressed in the future is, of course, whether image-based assessment of parameters of bone strength represents valid surrogate estimates of fracture susceptibility and whether the technology is transferable to typical fracture sites.

Acknowledgments

## Bibliography and References Cited

1. Schuit SC, van der Klift M, Weel AE, de Laet CE, Burger H, Seeman E, Hofman A, Uitterlinden AG, van Leeuwen JP, Pols HA. Fracture incidence and association with bone mineral density in elderly men and women: the Rotterdam Study. Bone 2004;34(1):195–202. [PubMed: 14751578]

2. Stone KL, Seeley DG, Lui LY, Cauley JA, Ensrud K, Browner WS, Nevitt MC, Cummings SR. BMD at multiple sites and risk of fracture of multiple types: long-term results from the Study of Osteoporotic Fractures. J Bone Miner Res 2003;18(11):1947–1954. [PubMed: 14606506]

3. Assessment of fracture risk and its application to screening for postmenopausal osteoporosis. Report of a WHO Study Group; World Health Organ Tech Rep Ser. 1994. p. 1-129.

4. Siris ES, Brenneman SK, Barrett-Connor E, Miller PD, Sajjan S, Berger ML, Chen YT. The effect of age and bone mineral density on the absolute, excess, and relative risk of fracture in

postmenopausal women aged 50–99: results from the National Osteoporosis Risk Assessment (NORA). Osteoporos Int 2006;17(4):565–574. [PubMed: 16392027]

5. Benito M, Gomberg B, Wehrli FW, Weening RH, Zemel B, Wright AC, Song HK, Cucchiara A, Snyder PJ. Deterioration of trabecular architecture in hypogonadal men. J Clin Endocrinol Metab 2003;88(4):1497–1502. [PubMed: 12679429]

6. MacNeil JA, Boyd SK. Load distribution and the predictive power of morphological indices in the distal radius and tibia by high resolution peripheral quantitative computed tomography. Bone 2007;41(1):129–137. [PubMed: 17442649]

7. Boutry N, Cortet B, Dubois P, Marchandise X, Cotten A. Trabecular bone structure of the calcaneus: preliminary in vivo MR imaging assessment in men with osteoporosis. Radiology 2003;227(3):708–717. [PubMed: 12676974]

8. Link TM, Vieth V, Matheis J, Newitt D, Lu Y, Rummeny EJ, Majumdar S. Bone structure of the distal radius and the calcaneus vs BMD of the spine and proximal femur in the prediction of osteoporotic spine fractures. Eur Radiol 2002;12(2):401–408. [PubMed: 11870442]

9. MacNeil JA, Boyd SK. Accuracy of high-resolution peripheral quantitative computed tomography for measurement of bone quality. Med Eng Phys 2007;29(10):1096–1105. [PubMed: 17229586]

10. Rajapakse CS, Magland J, Zhang XH, Liu XS, Wehrli SL, Guo XE, Wehrli FW. Implications of noise and resolution on mechanical properties of trabecular bone estimated by image-based finite-element analysis. J Orthop Res 2009;27(10):1263–1271. [PubMed: 19338030]

11. MacNeil JA, Doschak MR, Zernicke RF, Boyd SK. Preservation of periarticular cancellous morphology and mechanical stiffness in post-traumatic experimental osteoarthritis by antiresorptive therapy. Clin Biomech (Bristol, Avon) 2008;23(3):365–371.

12. Zhang XH, Liu XS, Vasilic B, Wehrli FW, Benito M, Rajapakse CS, Snyder PJ, Guo XE. In vivo microMRI-based finite element and morphological analyses of tibial trabecular bone in eugonadal and hypogonadal men before and after testosterone treatment. J Bone Miner Res 2008;23(9):1426–1434. [PubMed: 18410234]

13. Kabel J, van Rietbergen B, Dalstra M, Odgaard A, Huiskes R. The role of an effective isotropic tissue modulus in the elastic properties of cancellous bone. J Biomech 1999;32(7):673–680. [PubMed: 10400354]

14. Ladd AJ, Kinney JH, Haupt DL, Goldstein SA. Finite-element modeling of trabecular bone: comparison with mechanical testing and determination of tissue modulus. J Orthop Res 1998;16(5):622–628. [PubMed: 9820288]

15. van Rietbergen B. Micro-FE analyses of bone: state of the art. Adv Exp Med Biol 2001;496:21–30. [PubMed: 11783621]

16. Wald MJ, Magland JF, Rajapakse CS, Wehrli FW. Structural and Mechanical Parameters of Trabecular Bone Estimated From In Vivo High-Resolution Magnetic Resonance Images at 3 Tesla Field Strength. J Mag Reson Im. 2010

17. Arbenz P, van Lenthe GH, Mennel U, Muller R, Sala M. A scalable multi-level preconditioner for matrix-free mu-finite element analysis of human bone structures. International Journal for Numerical Methods in Engineering 2008;73(7):927–947.

18. Chung HW, Wehrli FW, Williams JL, Wehrli SL. Three-dimensional nuclear magnetic resonance microimaging of trabecular bone. J Bone Miner Res 1995;10(10):1452–1461. [PubMed: 8686500]

19. Magland JF, Wald MJ, Wehrli FW. Spin-echo micro-MRI of trabecular bone using improved 3D fast large-angle spin-echo (FLASE). Magn Reson Med 2009;61(5):1114–1121. [PubMed: 19215044]

20. Vasilic B, Wehrli FW. A novel local thresholding algorithm for trabecular bone volume fraction mapping in the limited spatial resolution regime of in vivo MRI. IEEE transactions on medical imaging 2005;24(12):1574–1585. [PubMed: 16353372]

21. Rajapakse CS, Wald MJ, Magland J, Zhang XH, Liu XS, Guo XE, Wehrli FW. Fast 3D registration of multimodality tibial images with significant structural mismatch. Proceedings of SPIE, Medical Imaging: Physiology, Function, and Structure from Medical Images 2009;7262 72620O.

22. Magland JF, Rajapakse CS, Wald MJ, Vasilie B, Guo XE, Zhang XH, Wehrli FW. Grayscale MR Image Based Finite Element Mechanical Modeling of Trabecular Bone at In Vivo Resolution. Journal of Bone and Mineral Research 2008;23:S310-S.

23. Rajapakse CS, Magland JF, Wald MJ, Vasilic B, Zhang XH, Guo XE, Wehrli FW. Estimation of Relative Stiffness Contributions of Cortical and Trabecular Compartments by MRI-based Finite Element Analysis. Journal of Bone and Mineral Research 2008;23:S366-S.

24. Van Rietbergen B, Odgaard A, Kabel J, Huiskes R. Direct mechanics assessment of elastic symmetries and properties of trabecular bone architecture. J Biomech 1996;29(12):1653–1657. [PubMed: 8945668]

25. Saha PK, Wehrli FW. Measurement of trabecular bone thickness in the limited resolution regime of in vivo MRI by fuzzy distance transform. IEEE transactions on medical imaging 2004;23(1): 53–62. [PubMed: 14719687]

26. Magland JF, Wehrli FW. Trabecular bone structure analysis in the limited spatial resolution regime of in vivo MRI. Acad Radiol 2008;15(12):1482–1493. [PubMed: 19000865]

27. Homminga J, Huiskes R, Van Rietbergen B, Ruegsegger P, Weinans H. Introduction and evaluation of a gray-value voxel conversion technique. J Biomech 2001;34(4):513–517. [PubMed: 11266675]

28. Macneil JA, Boyd SK. Bone strength at the distal radius can be estimated from high-resolution peripheral quantitative computed tomography and the finite element method. Bone 2008;42(6): 1203–1213. [PubMed: 18358799]

29. Rockoff SD, Sweet E, Bleustein J. The relative contribution of trabecular and cortical bone to the strength of human lumbar vertebrae. Calcif Tissue Res 1969;3(2):163–175. [PubMed: 5769902]

30. Leonard MB, Zemel BS, Kawchak DA, Ohene-Frempong K, Stallings VA. Plasma zinc status, growth, and maturation in children with sickle cell disease. The Journal of pediatrics 1998;132(3 Pt 1):467–471. [PubMed: 9544903]

31. Black DM, Bilezikian JP, Ensrud KE, Greenspan SL, Palermo L, Hue T, Lang TF, McGowan JA, Rosen CJ. One year of alendronate after one year of parathyroid hormone (1–84) for osteoporosis. N Engl J Med 2005;353(6):555–565. [PubMed: 16093464]

32. Keaveny TM, Hoffmann PF, Singh M, Palermo L, Bilezikian JP, Greenspan SL, Black DM. Femoral bone strength and its relation to cortical and trabecular changes after treatment with PTH, alendronate, and their combination as assessed by finite element analysis of quantitative CT scans. J Bone Miner Res 2008;23(12):1974–1982. [PubMed: 18684084]

33. Bevill G, Keaveny TM. Trabecular bone strength predictions using finite element analysis of micro-scale images at limited spatial resolution. Bone 2009;44(4):579–584. [PubMed: 19135184]

34. Cao H, Ackerman JL, Hrovat MI, Graham L, Glimcher MJ, Wu Y. Quantitative bone matrix density measurement by water- and fat-suppressed proton projection MRI (WASPI) with polymer calibration phantoms. Magn Reson Med 2008;60(6):1433–1443. [PubMed: 19025909]

35. Anumula S, Magland J, Wehrli SL, Ong H, Song HK, Wehrli FW. Multi-modality study of the compositional and mechanical implications of hypomineralization in a rabbit model of osteomalacia. Bone 2008;42(2):405–413. [PubMed: 18053788]

36. Wehrli FW, Rajapakse CS, Magland JF, Snyder PJ. Mechanical implications of estrogen supplementation in early postmenopausal women. J Bone Miner Res. 2010
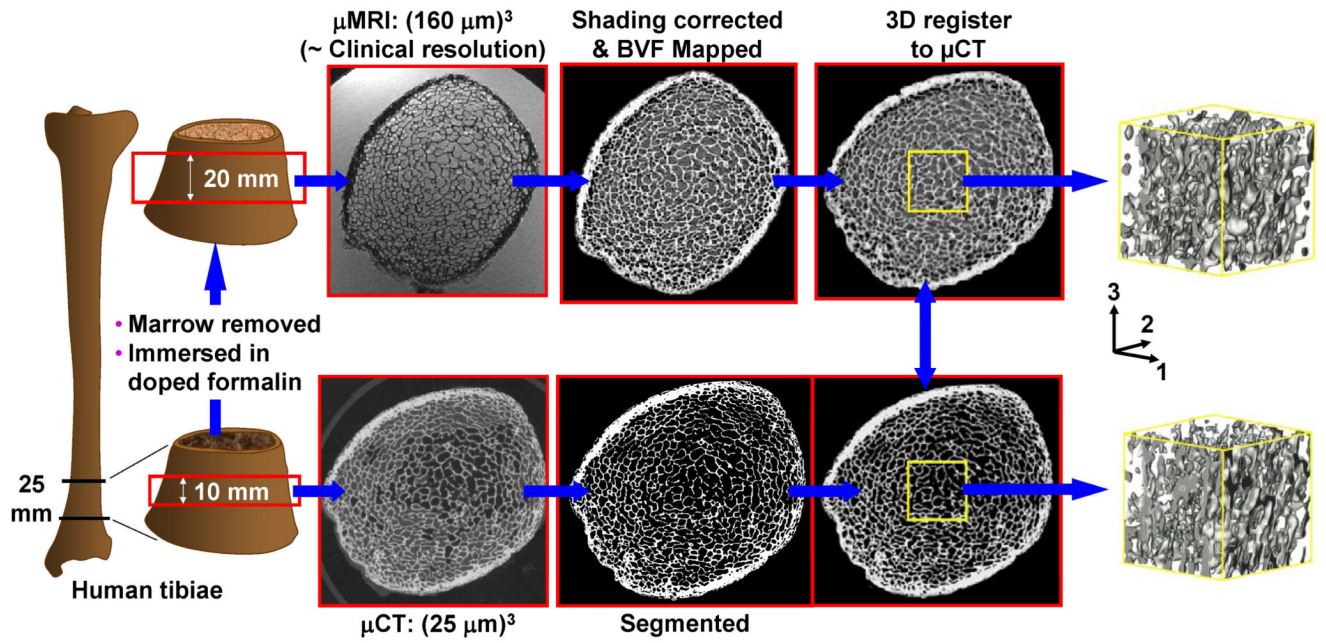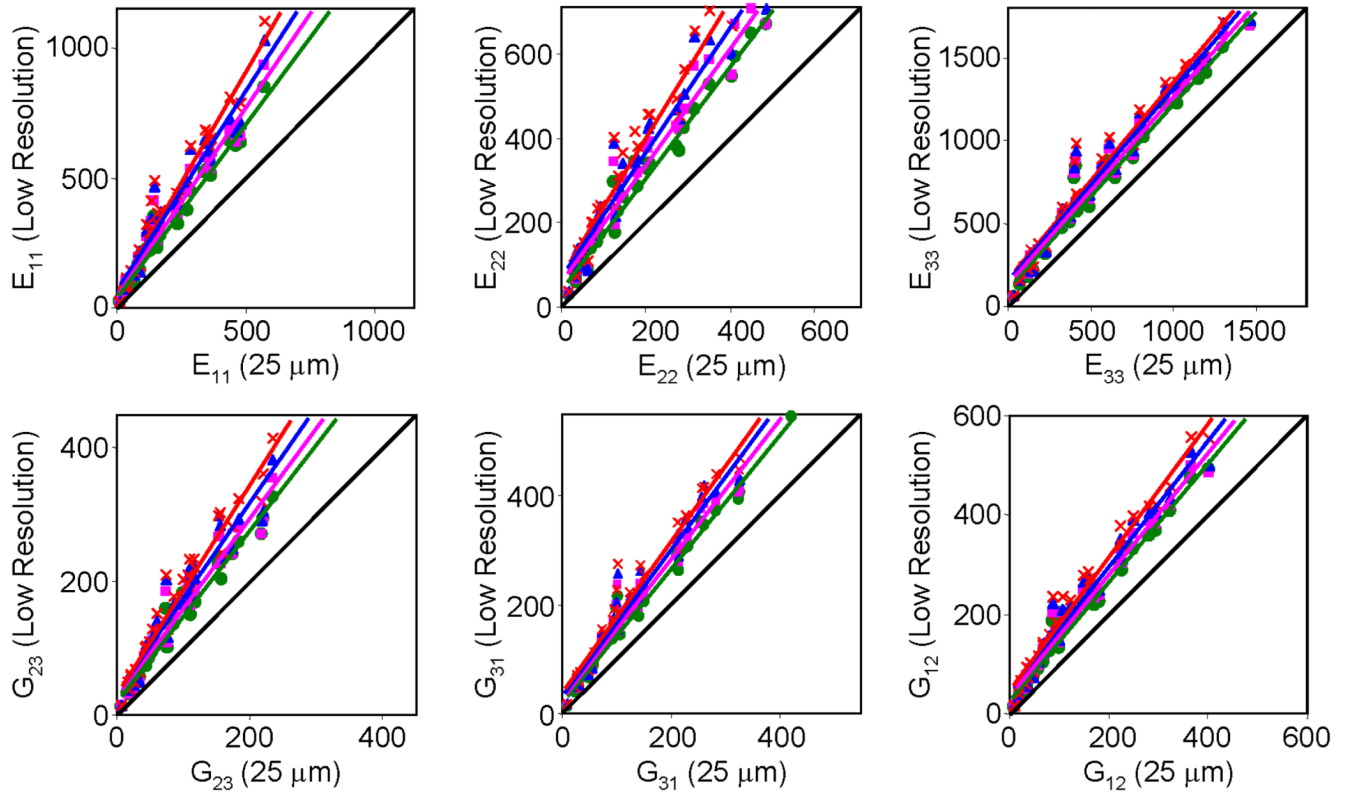
Figure 1.
Illustration of image acquisition and processing flow for validation of µMRI-based parameters against reference values derived on the basis of high-resolution µCT images.
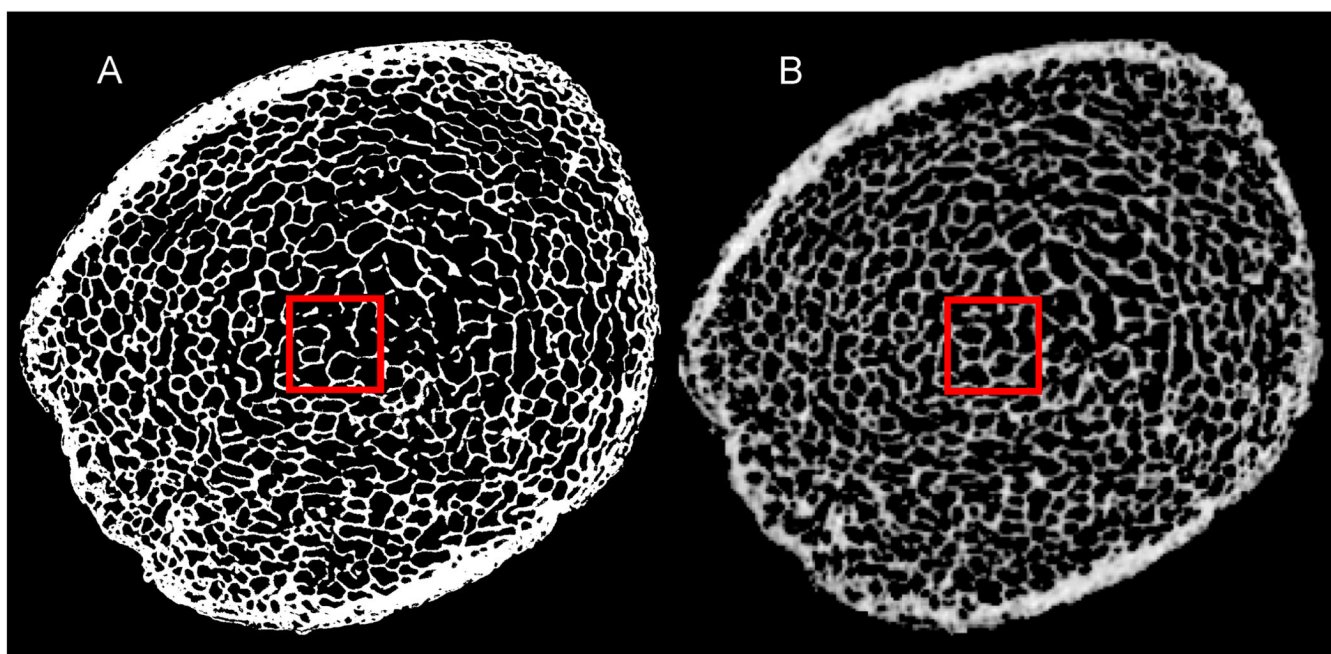
Figure 2.
Axial view of (A) reference µCT image at 25 µm and (B) 3D registered µMR BVF map at 160 µm isotropic voxel size, clearly showing close similarity in micro-structure with the (5 mm)^3 ROI used for µFE analysis indicated.
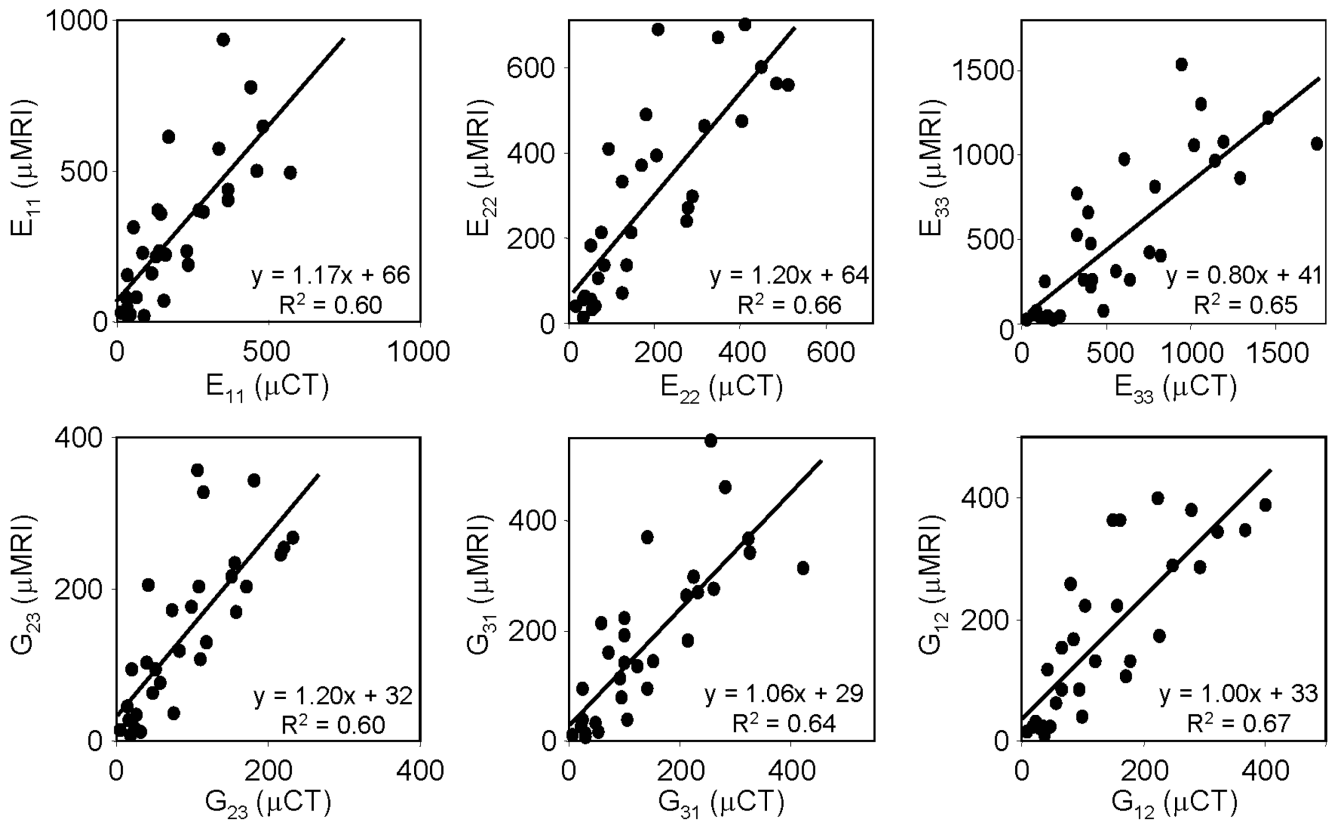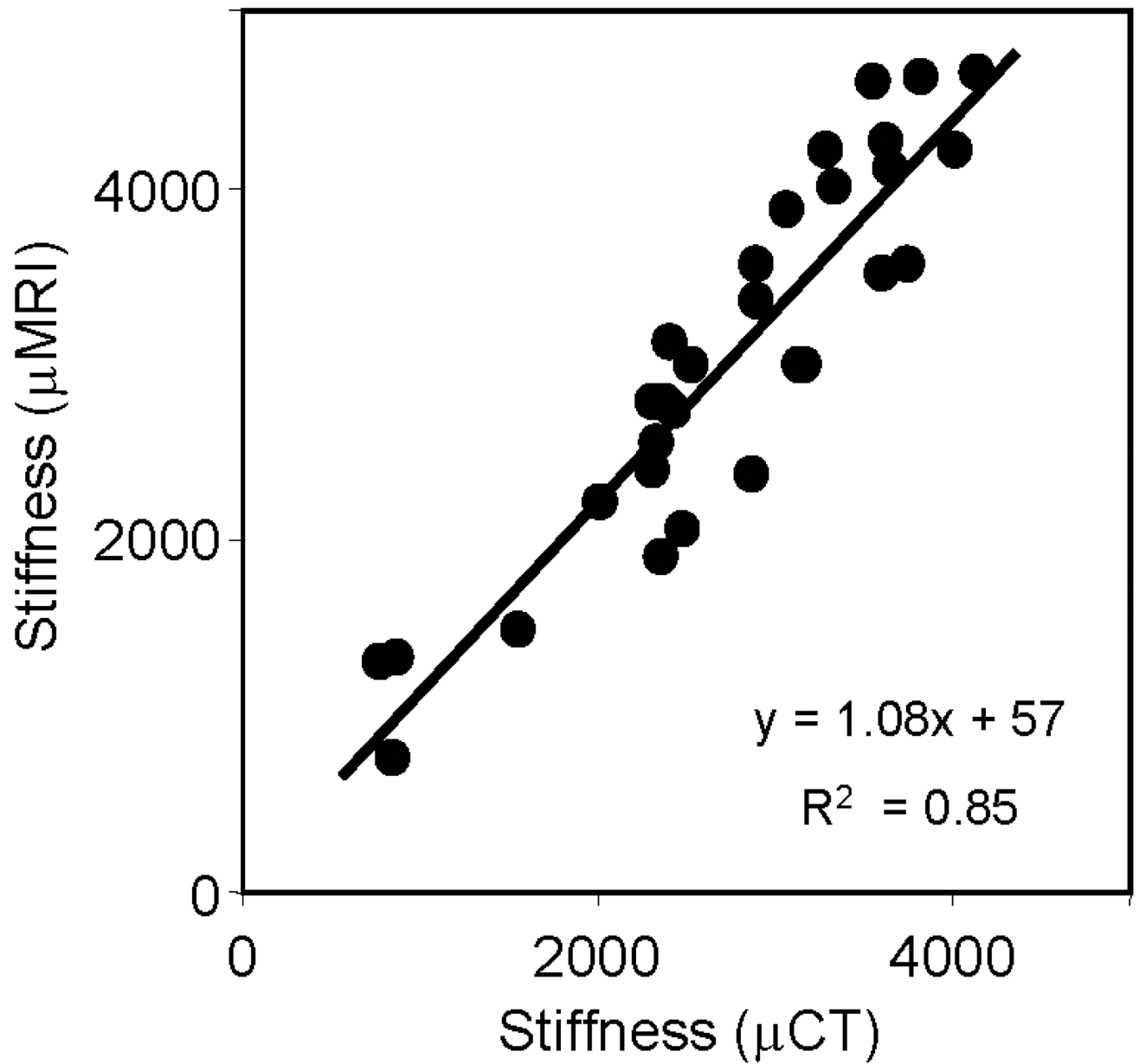
Figure 3.
Comparison of mechanical parameters (MPa) computed from (5 mm)^3 TB sub-regions on the basis of μMR images (160 µm isotropic voxel size) with those derived from volume-matched reference μCT images (25µm).
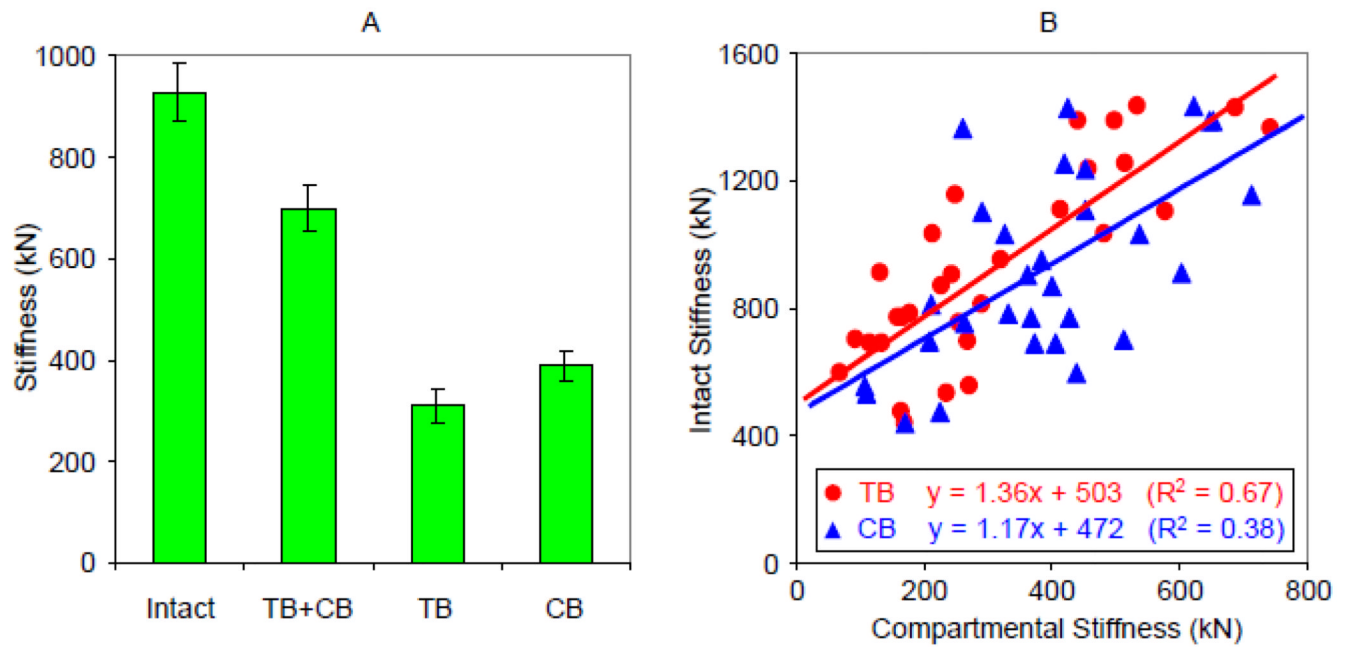
Figure 4.
Comparison of elastic moduli (MPa) computed from µCT images at 25 µm isotropic voxel size (abscissa) and corresponding values obtained after resampling the images to lower resolution: ● $(100 \ \mu m)^3$, ■ $(120 \ \mu m)^3$, ▲ $(140 \ \mu m)^3$, and ✕ $(160 \ \mu m)^3$. Diagonal line represents line of identity.

Figure 5.
Comparison of whole-bone sectional axial stiffness (MPa) computed from µMR images
(160 µm isotropic voxel size) with those derived from volume-matched reference µCT
images (25µm).

Figure 6.
(A) Average axial stiffness of tibia specimens computed from µMR images at 160 µm isotropic voxel size: individual compartment (TB and CB), both compartments intact, and sum of TB and CB compartments (TB+CB). (B) Relationship between intact whole-bone sectional stiffness and stiffness of individual compartments.

Table 1

Correlations between mechanical parameters derived from μCT images at 25 μm isotropic voxel size and corresponding values obtained after resampling to lower resolution. For all correlations, $p<0.0001$.

		100μm	120μm	140μm	160μm
E_{11}	R^2	0.97	0.95	0.94	0.95
	Slope/Intercept	1.35/37.90	1.44/51.18	1.55/61.46	1.69/63.34
E_{22}	R^2	0.98	0.96	0.95	0.96
	Slope/Intercept	1.33/39.97	1.39/58.08	1.48/70.42	1.64/71.54
E_{33}	R^2	0.98	0.97	0.97	0.97
	Slope/Intercept	1.12/10.93	1.14/131.37	1.17/145.63	1.19/160.10
G_{23}	R^2	0.97	0.94	0.93	0.95
	Slope/Intercept	1.29/18.35	1.35/25.88	1.43/31.31	1.57/30.93
G_{31}	R^2	0.98	0.97	0.97	0.97
	Slope/Intercept	1.22/24.31	1.27/29.74	1.33/34.01	1.39/38.45
G_{12}	R^2	0.98	0.97	0.97	0.97
	Slope/Intercept	1.20/25.79	1.23/34.12	1.28/40.19	1.36/42.75

Table 2

Structural properties (Tb.Th and BV/TV) of the 30 specimens, computed on the basis of 25µm µCT images from the same 5 mm × 5 mm × 5 mm trabecular bone sub-regions used for µFE analysis.

Structural Parameter	Mean	Minimum	Maximum
Tb.Th (µm)	71.45	39.89	105.32
BV/TV (%)	9.07	1.12	18.17